

https://dspace.org/

Characterization of methylammonium tin iodide thin films prepared by sequential physical vapour deposition

Margdaline Musanga Ligavo; Alex Sembito; Sizwe Sibiya; Sandile Thubane; Rudolph Erasmus ...

https://hdl.handle.net/10539/42093
WOS

Downloaded from a DSpace repository. https://dspace.org/

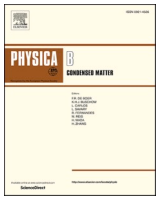
Physica B 695 (2024) 416496



Contents lists available at ScienceDirect

Physica B: Condensed Matter

journal homepage: www.elsevier.com/locate/physb





Characterization of methylammonium tin iodide thin films prepared by sequential physical vapour deposition

Margdaline Musanga Ligavo [a,b], Alex Sembito [a,b], Sizwe Sibiya [b], Sandile Thubane [b], Sebastian Waita [a], Francis Wanjala Nyongesa [a], Rudolph Erasmus [c], Mmantsae Diale [b,*]

[a] Department of Physics, University of Nairobi, P. O. Box 30197, 00100, Nairobi, Kenya
[b] Department of Physics, University of Pretoria, Private Bag X20, Hatfield, 0028, South Africa
[c] School of Physics, University of the Witwatersrand, Private Bag 3, Wits, 2050, Johannesburg, South Africa

ARTICLE INFO

Keywords:
Sequential physical vapour deposition
Methylammonium tin triiodide
Perovskites

ABSTRACT

Methylammonium tin triiodide ($MASnI_3$) films were grown through Sequential Physical Vapour Deposition (SPVD) without breaking the vacuum and optimized by varying MAI thickness and annealing time while keeping SnI_2 thickness constant. The film's crystallinity increased with MAI thickness and annealing time. Optimal bandgap was attained for the film with 500 nm MAI annealed for 20 & 40 min. FE-SEM revealed densely packed, large grains, increasing in size with MAI thickness and on annealing from 0 to 40 min and decreasing at 80 min. The film with 300 nm MAI thickness annealed for 40 min showed the strongest PL intensity suggesting reduced carrier recombination losses. Trap densities reduced with annealing time and MAI thickness due to improvements in films' crystallinity, grain sizes and reduced grain boundaries which act as carrier trapping sites. Hence, films prepared through SPVD, exhibit excellent structural, optical, and morphological properties, suitable for photovoltaic applications.

1. Introduction

Recent years have seen a greater research interest in organic-inorganic halide perovskite (OIHPs) materials because of their outstanding optoelectronic properties, including long carrier diffusion length, strong light absorption, tunable bandgap, and prolonged carrier lifespan. The power conversion efficiency (PCE) of OIHP solar cells has risen dramatically from 3.80 % to about 26.00 % for over a decade [1]. However, their commercialization and large-scale production are inhibited by toxic lead (Pb), amongst other factors, including instability and reproducibility [2]. The degradation of lead-based OIHP solar cells can lead to environmental contamination of groundwater, soil, and air [3]. Various elements such as germanium (Ge) [4], copper (Cu) [5], tin (Sn) [6], bismuth (Bi) [7], and antimony (Sb) [8] have been explored as possible alternatives to lead (Pb) in OIHPs solar cells. Amongst these, Sn and Ge are considered the most suitable due to their comparable electronic configuration and ionic radii with that of Pb [9]. Moreover, Sn is less toxic than Pb and Sn-based perovskites' optical bandgap ranges from 1.20 to 1.40 eV which nears the optimum bandgap of 1.34 eV provided by the Shockley–Queisser (SQ) limit under the 1.50 a.m. solar spectrum [10]. Their theoretical efficiency can exceed 33 % at an ideal open circuit voltage (V_{oc}) of 1.1 V [11]. Hence tin-based perovskites are considered promising candidates for efficient photovoltaic application.

Many successful ways to enhance the stability of Sn-based perovskite solar cells have been established including morphology control [12], device and compositional engineering [13] and introduction of reducing reagents [14]. For instance, Ryu et al. [15] prepared Sn-based perovskite with improved film morphology by the addition of L–Asparagine additive that enhanced the device PCE from 10.54 to 13.31 %. Sn-based perovskite with triple cations of the form $FA_{0.55}$ $MA_{0.4}$ $Cs_{0.05}$ $Sn_{0.6}Pb_{0.4}I_3$ was designed by Gunasekaran et al. [16]. The device displayed high stability and a PCE of over 22 % was obtained. Sanchez et al. [17] demonstrated stability and efficiency improvement of Sn perovskite by incorporating dipropyl ammonium iodide and sodium borohydride reducing agents in the precursor. The device showed a high PCE of over 10 % and improved stability of over 13 h.

Despite the impressive advancements, Sn-based OIHPs still lag behind their Pb–based counterparts due to their susceptibility to oxidation, particularly from Sn^{2+} to Sn^{4+}, generating films with high electrical conductivity and large hole-doping concentrations, producing

* Corresponding author.
E-mail address: Mmantsae.diale@up.ac.za (M. Diale).

https://doi.org/10.1016/j.physb.2024.416496
Received 6 June 2024; Received in revised form 20 August 2024; Accepted 3 September 2024
Available online 8 September 2024
0921-4526/© 2024 Published by Elsevier B.V.

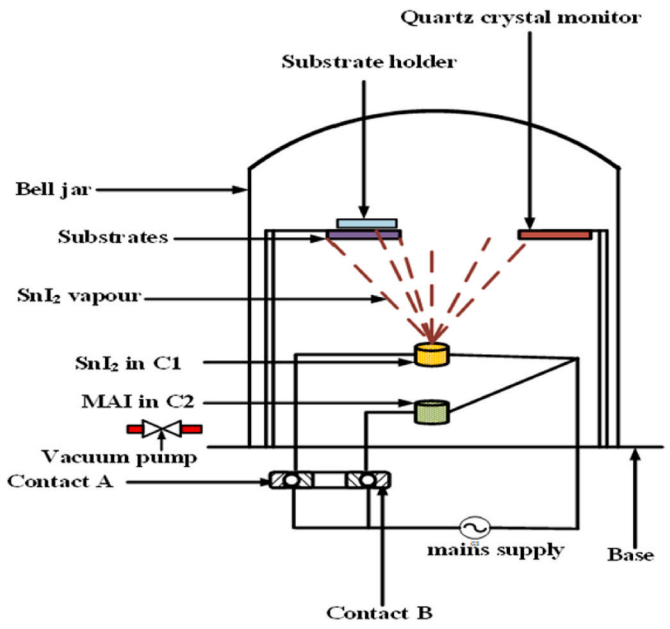


Fig. 1. Experimental set-up for sequential physical vapour deposition of SnI_2 and MAI single layers.

poor photovoltaic performance and short-circuit behaviour [18]. In addition, Sn-based perovskites tend to crystallize more quickly either during spin coating or at room temperature, thus hindering the uniform growth of the films. Films with randomly oriented growth are frequently generated through the one-step spin–coating solution processing method, which results in inadequate surface coverage [19]. Therefore, there is a need to develop improved techniques for growing Sn-based perovskites with superior-quality films [20]. The advantages of solution processing include simplicity and the ability to introduce additives into the precursor [21]. On the other hand, thermal vapour deposition uses non-toxic solvents [22], at times, it requires no post-annealing of the films [23], and several layers of films can be deposited without inflicting damage on them [24]. Among the thermal vapour deposition methods, high vacuum SPVD has successfully been employed to deposit perovskite films. SPVD offers control over crystallization, improved surface coverage, and uniformity due to the capacity to regulate the deposition rate and film thickness [25]. A few published works on Sn-based OIHPs produced through physical vapour deposition (PVD) have been reported. Arend et al. [26] prepared $MASnI_3$ thin films through SPVD where the rate of deposition was controlled by monitoring the SnI_2 current and MAI temperature. Although films produced were of better morphology, reproducibility was difficult as a result of changing deposition rate, due to highly volatile MAI. Yu et al. [27] prepared $MASnI_3$ films via co-evaporation, without annealing. SnI_2 and MAI were deposited in the vacuum controlling the rate of SnI_2 while keeping the pressure of MAI constant. This approach poses the challenge of reproducing $MASnI_3$ stoichiometry due to difficulty in maintaining controlled parameters throughout the deposition period. Other studies have incorporated SPVD with solution method, whereby SnI_2 is evaporated in a vacuum followed by spin-coating MAI. The resulting perovskite films displayed full surface coverage [28]. Very few reports exist in literature about growing $MASnI_3$ films through SPVD, particularly without breaking the vacuum which minimizes oxidation of Sn^{2+} to Sn^{4+}. Moreover, to the best of our knowledge, there are no reports illustrating the growth of $MASnI_3$ films and optimization of its thickness and annealing time through SPVD. In addition, film reproducibility is greatly enhanced because the thicknesses of the precursors are controlled through a crystal monitor rather than relying on the rate of deposition as reported in other studies. The results obtained in this work provide the optimal film thickness and annealing time suitable to obtain superior structural, optical, and morphological properties for photovoltaic application.

2. Experimental

2.1. Materials

MAI (99.99 % purity) and SnI_2 (99.999 % purity) powders were purchased from Sigma Aldrich and used without additional purification. $PC_{70}BM$ with 95 % purity and Tin IV oxide powder with 99.9 % purity were purchased from Ossila and Sigma Aldrich respectively.

2.2. Perovskite film deposition

FTO glass substrates were sliced into 15 mm × 20 mm, and then cleaned by ultrasonication in detergent, acetone, isopropanol and deionized water for 20 min each and dried with nitrogen gas. The substrates were then transferred to a UV-ozone cleaner for 15 min, to remove surface contaminants and mounted inside the resistive evaporator as shown in Fig. 1. Boron nitride crucibles, C1 and C2 were filled with SnI_2 and MAI powders, respectively. The system was evacuated to a pressure of $\approx 6x10^{-5}$ mbar at the start of SnI_2 deposition then reached $\approx 10^{-6}$ mbar at the end of MAI deposition. SnI_2 and MAI layers' sequential deposition was achieved using contacts A and B without breaking the vacuum. SnI_2 was deposited at a rate of between 0.2 and 0.5 Å/s while MAI at 0.6–1.5 Å/s. The temperature of the chamber was measured using a digital thermometer and was observed to rise from 25 °C at the start of SnI_2 deposition to 28.5 °C at the end of MAI deposition. The film's thickness was regulated by a Quartz crystal monitor. SnI_2 thickness was kept at 100 nm, and MAI was varied in steps of 300 nm, 400 nm, and 500 nm. Annealing of the perovskite films was done under the flow of nitrogen gas at 80 °C for varying times.

2.3. Electron-only device fabrication

To fabricate FTO/SnO_2/perovskite/$PC_{70}BM$/Au electron–only device, 100 nm of SnO_2 was deposited on clean FTO substrates in the resistive evaporator and then annealed at 150 °C for 30 min. The substrates were then ozone cleaned for 15 min and loaded in the resistive evaporator where sequential deposition of SnI_2 and MAI was done. The films were then annealed for 20, 40 and 80 min under nitrogen flow and then returned inside the chamber where 70 nm of $PC_{70}BM$ and 80 nm of gold (Au) were subsequently deposited.

2.4. Film characterization

Morphological properties of the prepared $MASnI_3$ films were characterized using the field emission scanning electron microscope (FE–SEM Zeiss Crossbeam 540 ultra). The grain sizes of the particles were determined using the Image J software. The X-ray diffraction (XRD) spectra of the films were measured by a Rikagu Smart H150–2100 diffractometer using the Cu Kα radiation with a wavelength of 1.5406. The film's optical absorption was obtained by a Cary 60 UV–Vis spectrometer from Agilent technologies. Photoluminescence (PL) emission of the films was examined using indium gallium arsenide (InGaAs) R2658 Vis-NIR PMT detector with an excitation wavelength of 400 nm.

2.5. J-V characteristics

Electrical measurements were done using the ORIEL LCS-100 solar simulator and Agilent B2912 source meter A.M 1.5 and 1 sun illumination ($1000W/m^2$) based on space the charge limited current (SCLC) technique. Newport 91150 V silicon reference cell was used for calibration.

Table 1
lattice constants obtained at different MAI thickness.

MAI thickness (nm)	a (Å)	b (Å)	b (Å)	Cell volume (Å^3)
300	8.76	8.76	12.38	951.15
400	8.76	8.76	12.45	955.10
500	8.78	8.78	12.45	960.61
Standard from COD	8.73	8.73	12.50	952.20

3. Results and discussion

3.1. Structural properties of $MASnI_3$

XRD measurements revealed diffraction peaks located at 2θ corresponding to 14.28°, 24.95°, 28.68°, 32.22°, 41.10°, and 51.06°, indexed to (110), (202),(220), (222), (400) and (404) crystal planes, respectively, and matched the tetragonal structure of space group *I4/mcm* using the crystallographic database COD: 7015449 [18]. The lattice constants of the crystal system were calculated based on equations (1) and (2) [29] using peaks at 2θ = 14.28° and 28.68°.

$$n\lambda = 2d \sin\theta \tag{1}$$

$$\frac{1}{d^2} = \frac{h^2 + k^2}{a^2} + \frac{l^2}{c^2} \tag{2}$$

Where n = 1 for first order diffraction, λ = 0.15406 nm for Cu Kα wavelength, h, k, l are Miller indices while a and c are lattice parameters. The lattice parameters computed for films with varying MAI thickness annealed at 80 °C for 40 min are consistent with earlier reported literature [30–32]. Table 1 shows the changes in lattice parameters in relation to MAI thickness.

3.1.1. Effect of annealing and MAI thickness on the crystallinity of $MASnI_3$ films

Fig. 2(a) and (b) shows X-ray diffractograms of $MASnI_3$ films obtained for different annealing times and MAI thicknesses respectively. The intensity of the peaks increased with annealing time and MAI thickness. This indicates that the crystallization of the film was not complete inside the deposition chamber due to the low temperature measured at 28.50 °C, necessitating annealing. $MASnI_3$ films prepared showed a strong inclination along the (110) and (220) planes, in agreement with reported work [26,28,29].

$MASnI_3$ perovskite consisting of 500 nm of MAI thickness was annealed for 0, 20, 40 and 80 min, to investigate how annealing time affects crystallinity. It is observed in Fig. 2(a) that a pure $MASnI_3$ crystal structure of space group *I4/mcm* exists for the as-deposited film, implying that the perovskite began to form inside the deposition chamber, and annealing only improved its crystallinity. Additional peaks due to the presence of SnI_2 were observed at 2θ = 12.80° and 25.58°, respectively, when the film was annealed for 80 min, depicted in

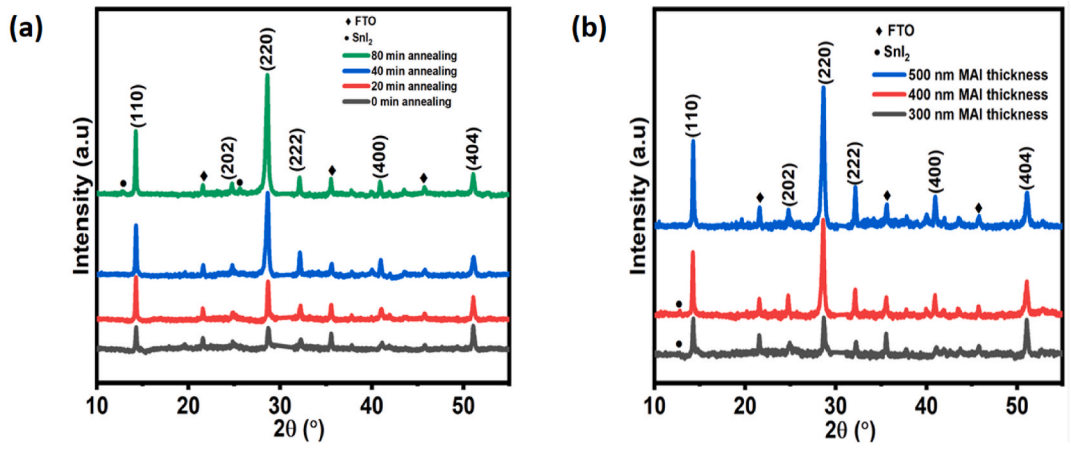


Fig. 2. (a) XRD diffractogram of $MSnI_3$ films with 500 nm of MAI annealed at different times, (b) XRD diffractogram of $MASnI_3$ films with varying thickness of MAI after annealing at 80°C for 40 min.

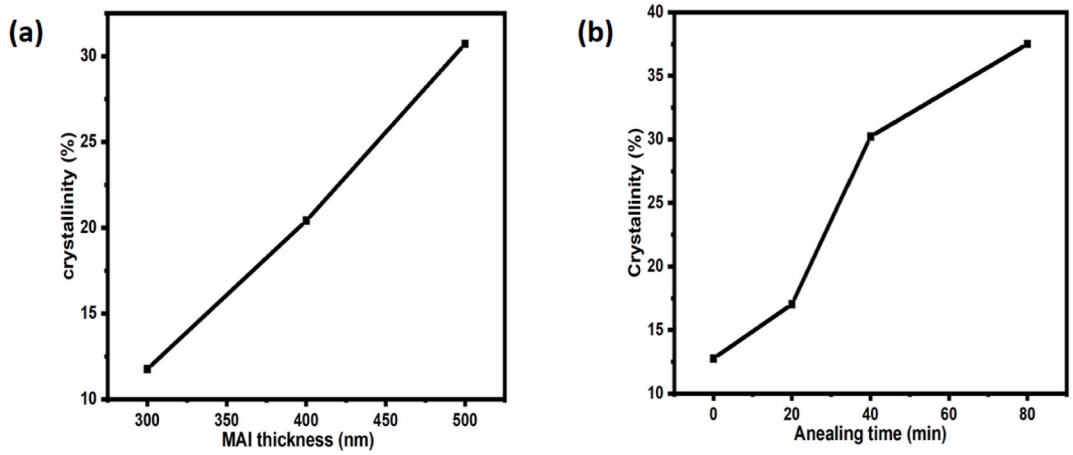


Fig. 3. (a)Variation of crystallinity of $MASnI_3$ film at 300 nm, 400 nm and 500 nm thickness of MAI; (b) plot of crystallinity of $MASnI_3$ film with 500 nm of MAI annealed at 80 °C for 0, 20, 40 and 80 min.

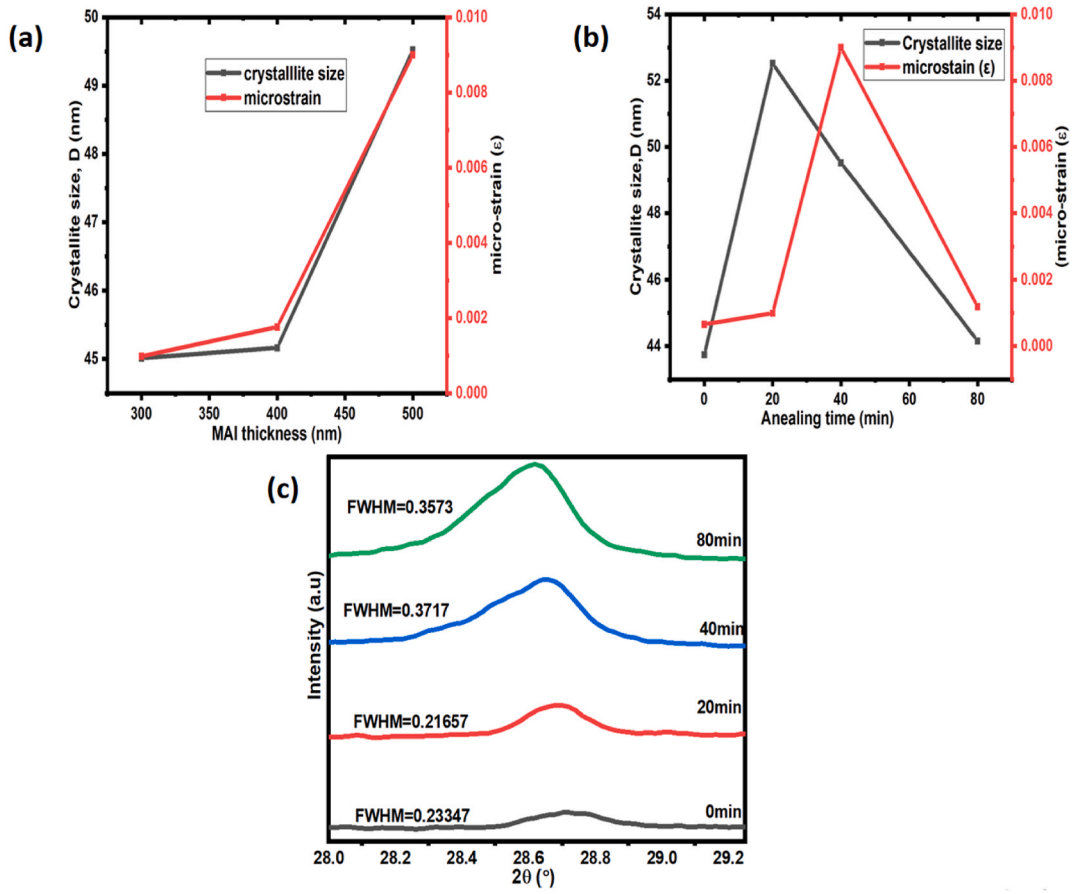


Fig. 4. (a) Crystallite size variation of $MASnI_3$ with 100 nm of SnI_2:300 nm, 400 nm and 500 nm of MAI thickness, (b) crystallite size variation of $MASnI_3$ film with 100 nm of SnI_2 and 500 nm of MAI, annealed for 0, 20,40 and 80 min, (c) Variation of FWHM width along the (220) peak for $MASnI_3$ films at various annealing times.

Fig. 2(a). This is attributed to decomposition of $MASnI_3$ due to the long exposure heat. $MASnI_3$ structure breaks down into its constituents, where MAI evaporates leaving behind SnI_2 seen in the spectra. Similar findings were reported by Ali et al. [33] Chen et al. [22] and Mehdi et al. [34] who studied the effect of annealing of $CH_3NH_3PbI_3$ and found that it decomposed upon heating at 130 °C, 120 °C and 110 °C, respectively. Hence the perovskite was not annealed beyond 80 min. Fig. 2(b) shows that the SnI_2 peak completely disappeared after annealing the film with 500 nm MAI thickness, indicating that a complete reaction of SnI_2 was achieved at 500 nm of MAI thickness.

The film's degree of crystallinity was calculated using XRD data in Origin Pro 2018 software based on the integration method defined by equation (3) [35].

$$\%\ crystallinity = \frac{Area\ under\ crystalline\ peaks}{Area\ under\ all\ peaks} \times 100 \tag{3}$$

The degree of crystallinity increased with the thickness of MAI, the highest being obtained at 500 nm as shown in Fig. 3(a). This was due to an increased reaction between SnI_2 and MAI as more MAI was consumed. A similar observation was made by Fru et al. [36] where $MAPbI_3$ films were synthesized via the SPVD technique.

Similarly, the crystallinity of the film was observed to increase with the annealing time as shown in Fig. 3(b). This behaviour is linked to improved interdiffusion of MAI into the SnI_2 layer as they get heated for a longer time, increasing the film's crystallization.

3.1.2. *Effect of annealing and MAI thickness on the film crystallite size and lattice strain*

The crystallite size was calculated in Origin Pro 2018 based on the Williamson–Hall (W–H) equation (4) [37].

$$\beta \cos\theta = \frac{k\lambda}{D} + 4\varepsilon \sin\theta \tag{4}$$

where D refers to the diameter of the crystallite, k is Scherrer's constant taken as 0.9 for spherical crystallites with cubic symmetry, λ is the wavelength of the X-ray used, in this case, Cu kα = 1.5406 Å, ε is the microstrain, β is full wave at half maximum width (FWHM) value and θ half of the corresponding Bragg's diffraction angle. According to the Williamson -Hall plot, the contribution to the total peak broadening in XRD diffraction is due to microstrain and crystallite size [38]. In this method, the y-intercept obtained from a graph of βcosθ against 4sinθ, gives the crystallite size while the microstrain component is the gradient of the plot. The crystallite size and microstrain of $MASnI_3$ films increased with MAI's thickness, attributed to volume increase as MAI intercalates into the film as shown in Fig. 4(a). These results are consistent with those obtained by Kumar et al. [39] where the impact of crystallite size and lattice strain on perovskite was assessed. They found that as crystallite size increased, the lattice strain increased as well because the particle–to–particle bond length decreased.

The crystallite size of the $MASnI_3$ film increased with annealing time from 0 to 20 min and then decreased from 20 to 80 min, as shown in Fig. 4(b). The reduction of the crystallite size is due to the broadening of the peak along the (220) plane, as shown in Fig. 4(c), and in reference to the famous Scherrer equation (5) [37].

$$\beta = \frac{k\lambda}{D\cos\theta} \tag{5}$$

where β is the FWHM width, k is the Scherrer constant, D is crystallite size, and λ is the wavelength. From the equation, the crystallite size

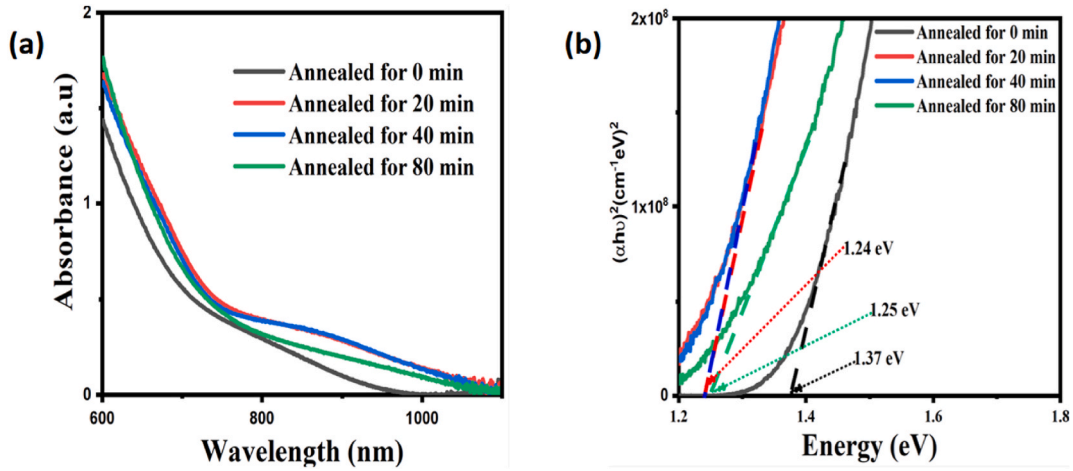


Fig. 5. (a) UV–vis absorption spectra; and (b) Tauc plot of $MASnI_3$ films with 500 nm of MAI thickness annealed at 80 °C for varying times.

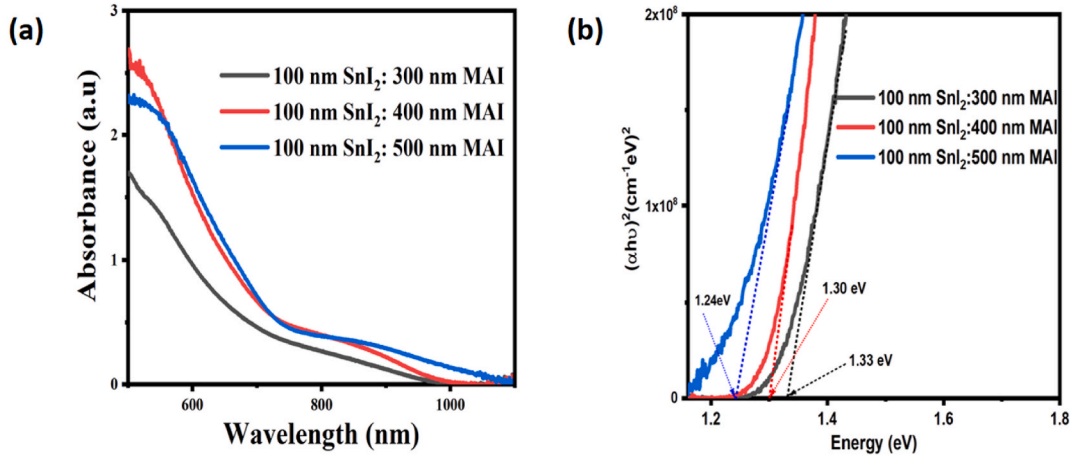


Fig. 6. (a) UV–vis absorption spectra; and (b) Tauc plot of $MASnI_3$ Perovskite thin film with varying MAI thickness annealed at 80 °C for 40 min.

varies inversely with FWHM of the peak. The microstrain increased slightly from 0 to 20 min annealing time and sharply increased from 20 to 40 min then decreased from 40 to 80 min. At 40 min annealing time, the crystallite size decreased despite the increase in the lattice strain due to the broadening of the peak along the (220) plane shown in Fig. 4(c). Moreover, the reduction of crystallite size at 80 min could be due to the decomposition of $MASnI_3$ as observed from the XRD peaks in Fig. 2(a) due to long–time exposure to heat.

3.2. Optical properties

3.2.1. UV–vis absorption of $MASnI_3$ films with varying MAI thickness and at different annealing times

Fig. 5 (a) shows the UV–vis absorption spectra of $MASnI_3$ perovskite thin films subjected to different times of annealing. All films displayed relatively strong absorption within the visible range. It was observed that absorption improved with annealing time from 0 to 60 min, above which it dropped. The increase in absorbance in the first 60 min of annealing indicates that SnI_2 and MAI interdiffusion was incomplete in the resistive evaporator, necessitating annealing to complete the reaction process. The incomplete reaction was due to the low temperature in the deposition chamber, measured at 28.50 °C. Bi et al. [40] investigated the impact of annealing time on the interdiffusion process of two stacked perovskite precursor layers of PbI_2 and MAI, each initially dried at 70 °C and 75 °C , respectively. Their studies revealed that the interdiffusion process was completed after an hour of thermal annealing at 105 °C. Thus, the increase in absorption from 0 to 60 min of annealing time attributed to improvement in the interdiffusion of the layers, resulting in improved crystallization, orientational growth and larger grain sizes.

Decreased absorption for the film annealed for 80 min is due to decomposition of the perovskite as observed in XRD (Fig. 2(a)). The optimal bandgap of 1.24 eV for $MASnI_3$ film was attained with the film annealed for 20 and 40 min, as shown in Fig. 5(b). Fig. 6(a) shows the UV–vis absorption spectra of the $MASnI_3$ films with different MAI thicknesses annealed for 40 min. The onset of absorption was red-shifted and the absorbance intensity enhanced as MAI thickness increased from 300 to 500 nm. The band gap of the grown films ranged from 1.33, 1.30 and 1.24 eV for 300, 400 and 500 nm of MAI thickness, respectively as depicted from the Tauc plot in Fig. 6(b). The band gap values obtained for all the films agree well with those reported in the literature [27,32,41], indicating that all the films exhibited a pure phase of $MASnI_3$ structure. The red-shift and, thus, the narrowing of the band gap as MAI thickness increase was due to the increase in the crystallite size, as supported by XRD results in Fig. 5(a). D'Innocenzo et al. [42] demonstrated that larger crystallites are associated with a smaller band gap and longer charge carrier lifetimes, positive for photovoltaic applications.

Above 500 nm of MAI thickness, the perovskite film absorption reduced and the band gap increased to 1.56 eV as shown in Figure S 1(a) & (b)of the supporting information. Rahimi et al. [43] explored the effect of excessive MAI regarding the performance of the perovskite films and devices prepared by spin coating. They found that having excess MAI could cause the formation of vacancies in the structure and may

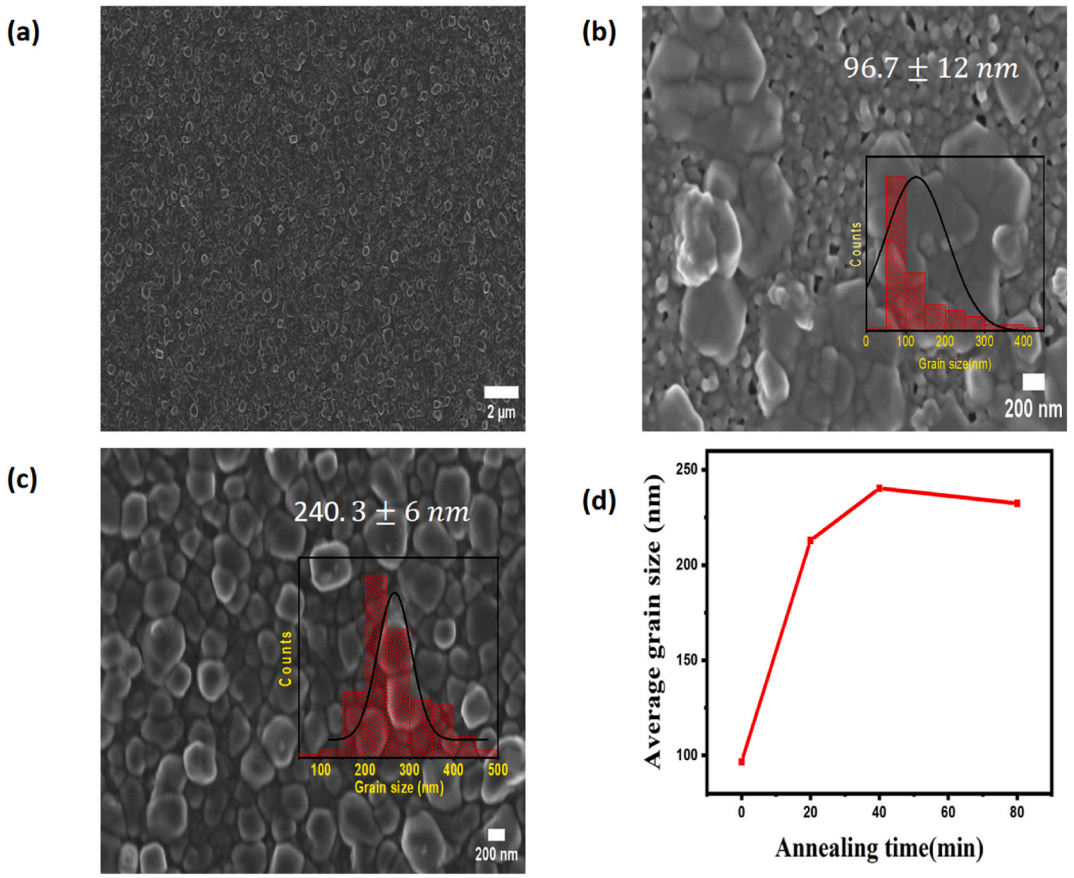


Fig. 7. (a) SEM image showing the surface coverage for the film annealed at 80 °*C*. FE-SEM images of $MASnI_3$ Perovskite thin films annealed for (b) 0 min. (c) 40 min. (d) Plot of the average grain size against annealing time for the perovskite film with 500 nm MAI thickness.

liberate halide ions, which then act as dopants affecting the perovskite's band gap. This explains the band gap changes with MAI thickness and poor optical absorption at 600 nm of MAI thickness. At 200 nm the film absorption was much lower with a band gap slightly higher than the optimal range of $MASnI_3$ as shown in Figure S1 (a) &(b) perovskite.

3.3. Morphological properties

Fig. 7(a) shows FE-SEM micrographs of $MASnI_3$ film top surface exhibiting minimal pinholes and uniform coverage. Incomplete crystallization, poor film growth and smaller average grain sizes of 96.70 nm were observed for the as-deposited film in Fig. 7(b). The interdiffusion and reaction process of the perovskite layers improved upon the film's thermal annealing for 40 min, as evidenced by the enlarged grain sizes of 240.30 nm, depicted in Fig. 7(c). However, the average grain sizes were slightly reduced to 212.0 nm upon annealing the film for 80 min, as displayed in Fig. 7(d).

Wang et al. [44] illustrated that the film gets infiltrated with moisture through grain boundaries; thus, the larger grain sizes that result from annealing are likely to improve the stability of the films. It can further be deduced that films with larger grain sizes degrade at a low rate due to limited chances of moisture and oxygen permeation. The slight decrease in the average grain size for annealing time at 80 min is due to the decomposition of the perovskite.

FE–SEM images in Fig. 8 (a) and 8 (b) and 8 (c) show the film morphology of $MASnI_3$ perovskite thin films with MAI thicknesses of 300, 400 and 500 nm, respectively. All the films are densely packed, homogeneous and exhibit minimum pinholes. The average grain size increased with MAI thickness, as illustrated in Fig. 8(d), conforming with previous literature on organic-inorganic halide perovskites [25]. The calculated grain sizes were 97, 109 and 240 nm for 300, 400 and 500 nm of MAI thickness, respectively which are bigger than those obtained by co-evaporation [27]. However, the obtained grain sizes in this study are still smaller than those reported for solution processing [29, 45]. The variation in the grain size for the different MAI thicknesses is consistent with the crystallite sizes obtained in Fig. 4(a).

The grains are oriented randomly and of varying sizes within the film, which is characteristic of polycrystalline materials. The primary cause of the grain size increase with MAI thickness is the availability of sufficient MAI to react with SnI_2 to form large $MASnI_3$ grains. Hence, the 500 nm MAI thickness film exhibits few grain boundaries. When the thickness of MAI was increased to 600 nm, the grain sizes reduced and the film exhibited many pin holes as illustrated in Fig. S2(b) of the supplementary information. At 200 nm of MAI thickness, the film was observed to peel off the substrates.

3.4. Photoluminescence emission

Fig. 9(a) shows the PL spectra of $MASnI_3$ films with different MAI thicknesses. It was observed that as MAI thickness increased from 300 to 500 nm, the PL intensity decreased. The peak wavelength for the film with 500 nm was slightly blue-shifted as shown in Table 2. Although more light absorption is expected in thicker films that could lead to stronger PL, a very thick absorber leads to low charge collection efficiency due to high rate of carrier recombination [46,47]. Hence, explaining the reduction of PL intensity when MAI exceeds 300 nm.

Fig. 9 (b) shows the PL spectra for both as-deposited $MASnI_3$ film and those annealed at 80 °C for 20, 40 and 80 min with 500 nm of MAI thickness. The peak wavelength for the as-deposited film was 963 nm, while that of films annealed for 20, 40, and 80 min was 938 nm, 940 nm

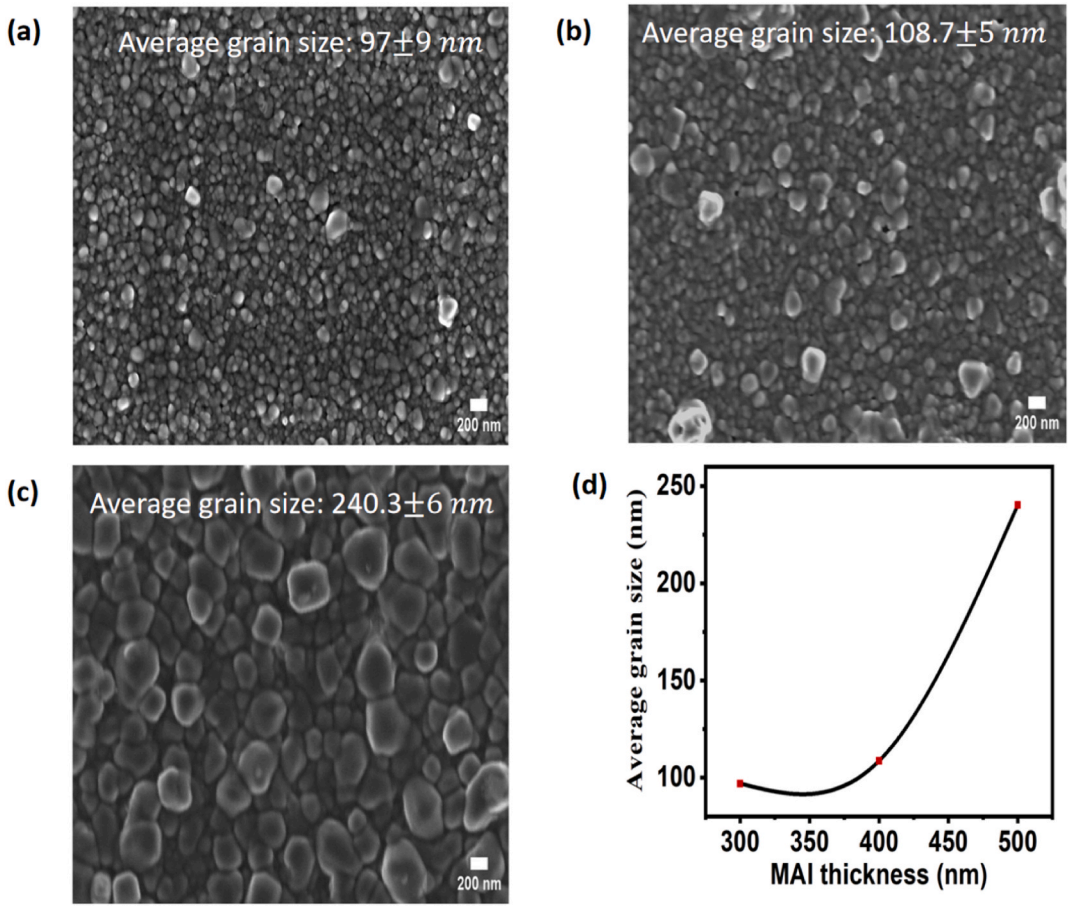


Fig. 8. (a) SEM images of $MASnI_3$ Perovskite thin film at various MAI thicknesses annealed at 80 °C for 40 min (a) 300 nm. (b) 400 nm, and (c) 500 nm of MAI thickness. (d) Average of grain size change with the thickness of MAI.

Table 2
PL emission wavelength for $MASnI_3$ film with varying MAI thickness and the respective bandgaps.

MAI thickness (nm)	PL emission, λ (nm)	Band gap from PL (eV)
300	950	1.31
400	950	1.31
500	940	1.32

and 946 nm, respectively, as shown in.

All the films showed varying emission intensity, with the one annealed at 40 min being the highest. The reduction of the PL intensity observed with the as-deposited film and the film annealed for 20 and 80 min is linked to their smaller grain sizes, which increases grain boundaries, thus providing avenues for non-radiative recombination losses due to shallow traps on the film surface. Dequilettes et al. [48] studied the PL decay dynamics of $MAPbI_3$ and found that PL intensity varied with

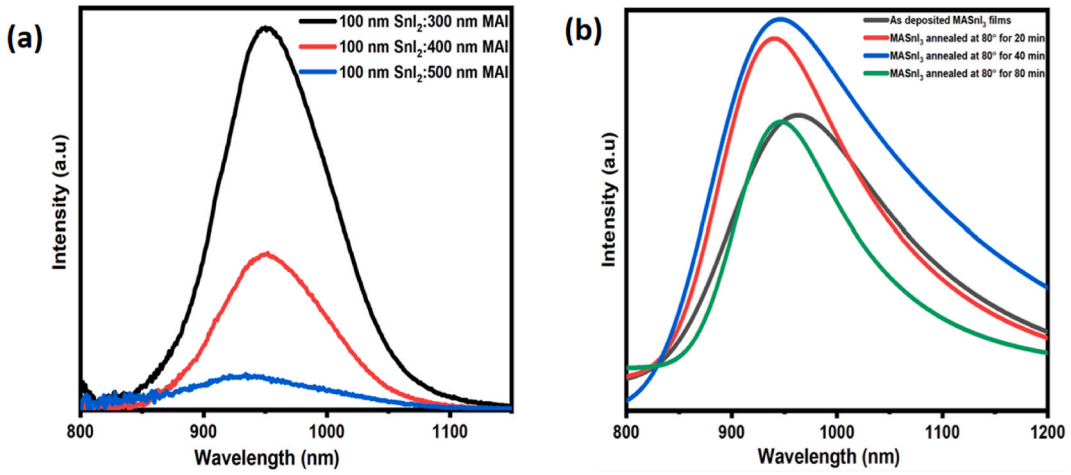


Fig. 9. PL spectra of (a) $MASnI_3$ with varying MAI thickness, (b) as–deposited $MASnI_3$ thin films with 500 nm of MAI thickness and films annealed at 80 °C for 20 min, 40 min and 80 min.

Table 3
PL emission wavelength and energy of $MASnI_3$ film with 500 nm of MAI thickness annealed at different times.

Annealing time (min)	PL emission, λ (nm)	Band gap from PL (eV)
0	963	1.29
20	938	1.32
40	940	1.32
80	946	1.31

different grains reducing at grain boundaries due to non-radiative recombination. The photoluminescence spectra were blue-shifted as the annealing time increased, as is typical of organo-metallic halide perovskites [26]. The blue-shift of the band gap is a result of the charge carriers filling the density of states as the films get annealed [49]. It can be deduced from Tables 2 and 3 that all $MASnI_3$ films with different MAI thicknesses and those annealed at varying times had a broad emission spectrum with a peak luminescence of ≈1.30 eV which agrees with previous studies [19,26,50].

3.5. Effect of MAI thickness and annealing time on trap state density

Fig. 10(a) and (b) show the dark J-V characteristics obtained for $MASnI_3$ films with varying MAI thicknesses and those annealed for different times respectively. The Inset of Fig. 10(a) shows the electron-only device structure used to obtain the J-V measurements. The graphs display a linear relation at low voltage bias indicating an ohmic characteristic of the device at a lower bias voltage. The current rises rapidly to a kink point which is the region where trap states are filled up by injected carriers in agreement with literature [51]. The J-V characteristics were used to examine the impact of perovskite thickness and annealing time on the electron trap densities (Nt) based on equation (6) [52].

$$N_t = \frac{2\varepsilon\varepsilon_o V_{TFL}}{qL^2} \tag{6}$$

where ε_0, ε, V_{TFL}, q and L refer to the vacuum dielectric constant (8.854 x10^{-12}CV^{-1}m^{-1}), Perovskite's dielectric constant, taken as 65 from literature [53], the value of the voltage at the onset of the trap-filled limited (TFL) regime, elementary charge (1.602x10^{-19}c) and thickness of the perovskite respectively. From equation (6), Nt depends on V_{TFL} value and the thickness of the film since other values are constants. It is observed in Fig. 10(a) that the values of V_{TFL} decreased as MAI thickness increased from 300 to 400 nm implying a decrease in the trap state densities. This phenomenon is due to the improvement of the crystallinity and grain size of the film with an increase in MAI thickness as seen in the XRD and FE-SEM results, which reduces the grain boundaries and pin holes that act as trapping sites. The calculated trap state densities were 5.878x10^{16} cm^{-3}, 2.056x10^{16}cm^{-3} and 1.3312x10^{16}cm^{-3} for 300, 400 and 500 nm MAI thickness respectively. These results agree well with those obtained by Fru et al. [25] where the trap densities of $MAPbBr_3$ decreased from 1.89x10^{16} cm^{-3} to 1.4x10^{16} cm^{-3} when the thickness of MABr increased from 400 to 500 nm.

There was a decrease in the values of V_{TFL} as the film was annealed from 0 to 40 min then slightly increased at 80 min. This translates to a decrease in the trap state densities as the film was annealed from 0 to 40 min, then slightly increased at 80 min. Similarly, this observation is attributed to the increase in grain size of the perovskite with annealing as shown in FE–SEM images which reduces pinholes and grain boundaries. The result shows that thermal annealing suppresses charge recombination losses. Computed Nt values were 2.106x10^{16} cm^{-3}, 1.451x10^{16} cm^{-3}, 1.331x10^{16} cm^{-3} and 1.394x10^{16} cm^{-3} for annealing times of 0,20,40 and 80 min respectively. Abbasi et al. [54] investigated the impact of annealing time on halide perovskite and found that an optimal amount of time is required for the complete conversion of precursors to high-purity perovskite and also found that overheating can induce defects in the film. This explains why annealing $MASnI_3$ films for 80 min leads to a slight increase in trap states. Hence the results show that 40 min is the optimal annealing time that leaves the film with minimal defect density. All the Nt values obtained at different MAI thicknesses as well as annealing times are in the range of those of halide perovskite (10^{15}–10^{17}cm^{-3}) [25,55,56].

4. Conclusion

In this work, the preparation of $MASnI_3$ films through sequential physical vapour deposition of SnI_2 and MAI has been demonstrated. Film optimization was achieved by fixing the thickness SnI_2 layer at 100 nm and varying MAI thickness and annealing time. The optical, structural and morphological properties changed with the annealing time and MAI thickness. The XRD diffractogram revealed a tetragonal structure with space group *I4/mcm*. It was observed that the degree of crystallinity increased with the thickness of MAI and annealing time. Crystallite size and lattice strain determined from the W-H plot increased with MAI thickness and annealing time from 0 to 20 min. The lattice strain reduced at 40 and 80 min of annealing, corresponding to a reduction in the crystallite size. The film showed strong absorption within the UV–vis region. The optimal bandgap was realized with the film containing 500 nm of MAI thickness annealed at 80 °C for 20 and 40 min. FE-SEM images illustrated high-quality films with full coverage, minimal pinholes and large grain sizes that increased on annealing. The largest grain sizes of 240 nm were obtained with 500 nm thickness of MAI and annealing at 80 °C for 40 min. The film with 300 nm MAI annealed for 40 min showed

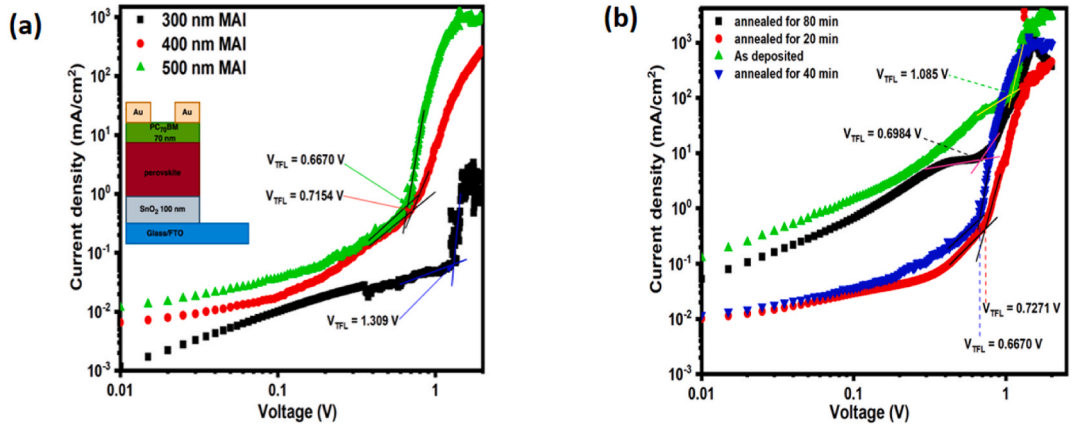


Fig. 10. Dark J – V characteristics of (a) $MASnI_3$ perovskite with different MAI thickness annealed at 80 °C for 40 min (inset is the electron-only device) (b) as-deposited $MASnI_3$ films and those annealed for 20,40 and 80 min. Graphs obtained by plotting logJ versus logV.

the strongest PL. Trap state densities are reduced with MAI thickness and annealing time. The structural, optical, and morphological properties depict that $MASnI_3$ made through the SPVD techniques is a good candidate for photovoltaic application.

CRediT authorship contribution statement

Margdaline Musanga Ligavo: Writing – original draft, Methodology, Formal analysis, Data curation, Conceptualization. **Alex Sembito:** Writing – original draft, Methodology, Formal analysis. **Sizwe Sibiya:** Writing – original draft. **Sandile Thubane:** Writing – original draft. **Sebastian Waita:** Writing – review & editing, Supervision. **Francis Wanjala Nyongesa:** Writing – review & editing, Supervision. **Rudolph Erasmus:** Writing – review & editing, Resources. **Mmantsae Diale:** Writing – review & editing, Supervision, Resources, Project administration, Funding acquisition.

Declaration of competing interest

The authors declare that they have no known competing financial interests or personal relationships that could have appeared to influence the work reported in this paper.

Data availability

Data will be made available on request.

Acknowledgement

The authors acknowledge the Partnership for Skills in Applied Sciences, Engineering & Technology (PASET)–Regional Scholarship and Innovation Fund (RSIF) Scholarship and partnership with the University of Pretoria (UP) and the University of Nairobi (UoN). UP Department of Physics provided access to the laboratories for fabrication and characterisation of the $MASnI_3$ films, the University of Witwatersrand, Department of Physics for access to the PL, and the South African Research Chair (SARCHI), UID 115463, funded by NRF/DSI.

Appendix A. Supplementary data

Supplementary data to this article can be found online at https://doi.org/10.1016/j.physb.2024.416496.

References

[1] M. Omrani, R. Keshavarzi, M. Abdi-Jalebi, P. Gao, Impacts of plasmonic nanoparticles incorporation and interface energy alignment for highly efficient carbon-based perovskite solar cells, Sci. Rep. 12 (2022) 5367, https://doi.org/10.1038/s41598-022-09284-9.

[2] T.D. Siegler, A. Dawson, P. Lobaccaro, D. Ung, M.E. Beck, G. Nilsen, L.L. Tinker, The path to perovskite commercialization: a perspective from the United States solar energy technologies office, ACS Energy Lett. 7 (2022) 1728–1734, https://doi.org/10.1021/acsenergylett.2c00698.

[3] M. Ren, X. Qian, Y. Chen, T. Wang, Y. Zhao, Potential lead toxicity and leakage issues on lead halide perovskite photovoltaics, J. Hazard Mater. 426 (2022) 127848.

[4] A.W. Azhari, F.S.X. Then, D.S.C. Halin, S. Sepeai, N.A. Ludin, Tin and germanium substitution in lead free perovskite solar cell: current status and future trends, in: IOP Conf. Ser. Mater. Sci. Eng., IOP Publishing, 2020 012057, https://doi.org/10.1088/1757-899X/957/1/012057.

[5] A. Lundmark, I. Ymén, Phosphate as a potential substitute for dichromate, when depressing galena in copper and lead separation, in: 29th Int. Miner. Process. Congr. IMPC 2018 17 Sept. 2018 21 Sept, 2018, 2019, pp. 1610–1618. https://www.diva-portal.org/smash/record.jsf?pid=diva2:1281061. (Accessed 4 October 2023).

[6] M.-C. Jung, S.R. Raga, Y. Qi, Properties and solar cell applications of Pb-free perovskite films formed by vapor deposition, RSC Adv. 6 (2016) 2819–2825, https://doi.org/10.1039/C5RA21291J.

[7] B. Yang, J. Chen, S. Yang, F. Hong, L. Sun, P. Han, T. Pullerits, W. Deng, K. Han, Lead-Free silver-bismuth halide double perovskite nanocrystals, Angew. Chem. 130 (2018) 5457–5461, https://doi.org/10.1002/ange.201800660.

[8] S. Wu, W. Li, J. Hu, P. Gao, Antimony doped lead-free double perovskites (Cs 2 NaBi 1- x Sb x Cl 6) with enhanced light absorption and tunable emission, J. Mater. Chem. C 8 (2020) 13603–13611, https://doi.org/10.1039/D0TC03003A.

[9] S. Tao, I. Schmidt, G. Brocks, J. Jiang, I. Tranca, K. Meerholz, S. Olthof, Absolute energy level positions in tin-and lead-based halide perovskites, Nat. Commun. 10 (2019) 2560, https://doi.org/10.1038/s41467-019-10468-7.

[10] J. Cao, F. Yan, Recent progress in tin-based perovskite solar cells, Energy Environ. Sci. 14 (2021) 1286–1325, https://doi.org/10.1039/D0EE04007J.

[11] W. Shockley, H.J. Queisser, Detailed balance limit of efficiency of p-n junction solar cells, J. Appl. Phys. 32 (1961) 510–519, https://doi.org/10.1063/1.1736034.

[12] L. Lei, M. Li, D.M. Grant, S. Yang, Y. Yu, J.A. Watts, D.B. Amabilino, Morphology and defect control of metal halide perovskite films for high-performance optoelectronics, Chem. Mater. 32 (2020) 5958–5972, https://doi.org/10.1021/acs.chemmater.0c00798.

[13] Z. Zhao, F. Gu, Y. Li, W. Sun, S. Ye, H. Rao, Z. Liu, Z. Bian, C. Huang, Mixed-organic-Cation tin iodide for lead-free perovskite solar cells with an efficiency of 8.12, Adv. Sci. 4 (2017) 1700204, https://doi.org/10.1002/advs.201700204.

[14] T.-B. Song, T. Yokoyama, C.C. Stoumpos, J. Logsdon, D.H. Cao, M.R. Wasielewski, S. Aramaki, M.G. Kanatzidis, Importance of reducing vapor atmosphere in the fabrication of tin-based perovskite solar cells, J. Am. Chem. Soc. 139 (2017) 836–842, https://doi.org/10.1021/jacs.6b10734.

[15] D.H. Ryu, N. Khan, J. Park, D. Paik, B.J. Kang, N.J. Jeon, S. Lee, H.K. Lee, S.K. Lee, W.S. Shin, J. Lee, H. Kim, K. Hong, S.H. Im, C.E. Song, Morphology and performance enhancement through the strong passivation effect of amphoteric ions in tin-based perovskite solar cells, Small 19 (2023) 2302418, https://doi.org/10.1002/smll.202302418.

[16] R.K. Gunasekaran, J. Jung, S.W. Yang, J. Yun, Y. Yun, D. Vidyasagar, W.C. Choi, C. Lee, J.H. Noh, D.H. Kim, S. Lee, High-throughput compositional mapping of triple-cation tin–lead perovskites for high-efficiency solar cells, InfoMat 5 (2023) e12393, https://doi.org/10.1002/inf2.12393.

[17] J. Sanchez-Diaz, R.S. Sánchez, S. Masi, M. Krečmarová, A.O. Alvarez, E.M. Barea, J. Rodriguez-Romero, V.S. Chirvony, J.F. Sánchez-Royo, J.P. Martinez-Pastor, Tin perovskite solar cells with> 1,300 h of operational stability in N2 through a synergistic chemical engineering approach, Joule 6 (2022) 861–883, https://doi.org/10.1016/j.joule.2022.02.014.

[18] Y. Takahashi, R. Obara, Z.-Z. Lin, Y. Takahashi, T. Naito, T. Inabe, S. Ishibashi, K. Terakura, Charge-transport in tin-iodide perovskite CH 3 NH 3 SnI 3: origin of high conductivity, Dalton Trans. 40 (2011) 5563–5568, https://doi.org/10.1039/c0dt01601b.

[19] F. Hao, C.C. Stoumpos, D.H. Cao, R.P. Chang, M.G. Kanatzidis, Lead-free solid-state organic–inorganic halide perovskite solar cells, Nat. Photonics 8 (2014) 489–494, https://doi.org/10.1038/NPHOTON.2014.82.

[20] T.-B. Song, Q. Chen, H. Zhou, C. Jiang, H.-H. Wang, Y.M. Yang, Y. Liu, J. You, Y. Yang, Perovskite solar cells: film formation and properties, J. Mater. Chem. A 3 (2015) 9032–9050, https://doi.org/10.1039/C4TA05246C.

[21] S. Liu, Y. Guan, Y. Sheng, Y. Hu, Y. Rong, A. Mei, H. Han, A review on additives for halide perovskite solar cells, Adv. Energy Mater. 10 (2020) 1902492, https://doi.org/10.1002/aenm.201902492.

[22] L.-C. Chen, C.-C. Chen, J.-C. Chen, C.-G. Wu, Annealing effects on high-performance CH3NH3PbI3 perovskite solar cells prepared by solution-process, Sol. Energy 122 (2015) 1047–1051, https://doi.org/10.1016/j.solener.2015.10.019.

[23] C. Roldán-Carmona, O. Malinkiewicz, A. Soriano, G.M. Espallargas, A. Garcia, P. Reinecke, T. Kroyer, M.I. Dar, M.K. Nazeeruddin, H.J. Bolink, Flexible high efficiency perovskite solar cells, Energy Environ. Sci. 7 (2014) 994–997, https://doi.org/10.1039/C3EE43619E.

[24] K. Tvingstedt, L. Gil-Escrig, C. Momblona, P. Rieder, D. Kiermasch, M. Sessolo, A. Baumann, H.J. Bolink, V. Dyakonov, Removing leakage and surface recombination in planar perovskite solar cells, ACS Energy Lett. 2 (2017) 424–430, https://doi.org/10.1021/acsenergylett.6b00719.

[25] J.N. Fru, N. Nombona, M. Diale, Synthesis and characterisation of methylammonium lead tri-bromide perovskites thin films by sequential physical vapor deposition, Phys. B Condens. Matter 578 (2020) 411884, https://doi.org/10.1016/j.physb.2019.411884.

[26] T.R. Arend, M. Tönnies, P. Reisbeck, C.J.P. Rieckmann, R. Kersting, Physical vapor deposition of methylammonium tin iodide thin films: physical vapor deposition of $CH_3NH_3SnI_3$ thin films, Phys. Status Solidi A 214 (2017) 1600796, https://doi.org/10.1002/pssa.201600796.

[27] Y. Yu, D. Zhao, C.R. Grice, W. Meng, C. Wang, W. Liao, A.J. Cimaroli, H. Zhang, K. Zhu, Y. Yan, Thermally evaporated methylammonium tin triiodide thin films for lead-free perovskite solar cell fabrication, RSC Adv. 6 (2016) 90248–90254, https://doi.org/10.1039/C6RA19476A.

[28] M. Weiss, J. Horn, C. Richter, D. Schlettwein, Preparation and characterization of methylammonium tin iodide layers as photovoltaic absorbers: methylammonium tin iodide layers as photovoltaic absorbers, Phys. Status Solidi A 213 (2016) 975–981, https://doi.org/10.1002/pssa.201532594.

[29] A. Bouich, J. Marí-Guaita, B.M. Soucase, P. Palacios, Manufacture of high-efficiency and stable lead-free solar cells through antisolvent quenching engineering, Nanomaterials 12 (2022) 2901, https://doi.org/10.3390/nano12172901.

[30] H. MallaHasan, Ö. Onay, Investigation of the effect of different factors on the performance of several perovskite solar cells: a simulation study by SCAPS, Eur. J. Eng. Sci. Technol. 5 (2022) 20–38, https://doi.org/10.33422/ejest.v5i1.927.

[31] M.M. Byranvand, W. Zuo, R. Imani, M. Pazoki, M. Saliba, Tin-based halide perovskite materials: properties and applications, Chem. Sci. 13 (2022) 6766–6781, https://doi.org/10.1039/D2SC01914K.

[32] Y. Dang, Y. Zhou, X. Liu, D. Ju, S. Xia, H. Xia, X. Tao, Formation of hybrid perovskite tin iodide single crystals by top-seeded solution growth, Angew. Chem. Int. Ed. 55 (2016) 3447–3450, https://doi.org/10.1002/anie.201511792.
[33] M. Ali Akhavan Kazemi, A. Jamali, F. Sauvage, A holistic study on the effect of annealing temperature and time on CH3NH3PbI3-based perovskite solar cell characteristics, Front. Energy Res. 9 (2021), https://doi.org/10.3389/fenrg.2021.732886.
[34] H. Mehdi, A. Mhamdi, A. Bouazizi, Effect of annealing treatment on the properties of inverted solar cells based on mixed halide perovskite, Phys. E Low-Dimens. Syst. Nanostructures 119 (2020) 114000, https://doi.org/10.1016/j.physe.2020.114000.
[35] R. Rotaru, M. Savin, N. Tudorachi, C. Peptu, P. Samoila, L. Sacarescu, V. Harabagiu, Ferromagnetic iron oxide–cellulose nanocomposites prepared by ultrasonication, Polym. Chem. 9 (2018) 860–868, https://doi.org/10.1039/C7PY01587A.
[36] J.N. Fru, N. Nombona, M. Diale, Characterization of sequential physical vapor deposited methylammonium lead tri-iodide perovskite thin films, Vacuum 182 (2020) 109727, https://doi.org/10.1016/j.vacuum.2020.109727.
[37] V.S. Vinila, J. Isac, Synthesis and structural studies of superconducting perovskite GdBa2Ca3Cu4O10. 5+ δ nanosystems, in: Des. Fabr. Charact. Multifunct. Nanomater., Elsevier, 2022, pp. 319–341. https://www.sciencedirect.com/science/article/pii/B9780128205587000224 (accessed November 14, 2023).
[38] A.U. Moreh, M. Momoh, H.N. Yahya, B. Hamza, I.G. Saidu, S. Abdullahi, Effect of thickness on structural and electrical properties of CuAlS2 thin films grown by two stage vacuum thermal evaporation technique, Int. J. Phys. Math. Sci. 8 (2016) 1084–1088, https://doi.org/10.5281/zenodo.2825178.
[39] D. Kumar, M. Singh, A.K. Singh, Crystallite size effect on lattice strain and crystal structure of Ba1/4Sr3/4MnO3 layered perovskite manganite, in: AIP Conf. Proc., AIP Publishing, 2018, https://doi.org/10.1063/1.5032520.
[40] C. Bi, Y. Shao, Y. Yuan, Z. Xiao, C. Wang, Y. Gao, J. Huang, Understanding the formation and evolution of interdiffusion grown organolead halide perovskite thin films by thermal annealing, J. Mater. Chem. A 2 (2014) 18508–18514, https://doi.org/10.1039/c4ta04007d.
[41] C. Gai, J. Wang, Y. Wang, J. Li, The low-dimensional three-dimensional tin halide perovskite: film characterization and device performance, Energies 13 (2020) 2, https://doi.org/10.3390/en13010002.
[42] V. D'Innocenzo, A.R. Srimath Kandada, M. De Bastiani, M. Gandini, A. Petrozza, Tuning the light emission properties by band gap engineering in hybrid lead halide perovskite, J. Am. Chem. Soc. 136 (2014) 17730–17733, https://doi.org/10.1021/ja511198f.
[43] F. Rahimi, S.P. Collins, C.S. Ferekides, A.M. Hoff, Methylammonium iodide and its effect as an intrinsic defect in perovskite structure and device performance, Org. Electron. 62 (2018) 304–310, https://doi.org/10.1016/j.orgel.2018.08.025.
[44] Q. Wang, B. Chen, Y. Liu, Y. Deng, Y. Bai, Q. Dong, J. Huang, Scaling behavior of moisture-induced grain degradation in polycrystalline hybrid perovskite thin films, Energy Environ. Sci. 10 (2017) 516–522, https://doi.org/10.1039/C6EE02941H.
[45] J. Marí-Guaita, A. Bouich, M.A. Shafi, A. Bouich, B. Marí, Investigation on the stability and efficiency of MAPbI $_3$ and MASnI $_3$ thin films for solar cells, Phys. Status Solidi A 219 (2022) 2100664, https://doi.org/10.1002/pssa.202100664.
[46] A. Bag, R. Radhakrishnan, R. Nekovei, R. Jeyakumar, Effect of absorber layer, hole transport layer thicknesses, and its doping density on the performance of perovskite solar cells by device simulation, Sol. Energy 196 (2020) 177–182, https://doi.org/10.1016/j.solener.2019.12.014.
[47] J. Zhang, T. Jiang, X. Zheng, C. Shen, X. Cheng, Thickness-dependent nonlinear optical properties of $CsPbBr_3$ perovskite nanosheets, Opt. Lett. 42 (2017) 3371–3374, https://doi.org/10.1364/OL.42.003371.
[48] D.W. De Quilettes, S.M. Vorpahl, S.D. Stranks, H. Nagaoka, G.E. Eperon, M. E. Ziffer, H.J. Snaith, D.S. Ginger, Impact of microstructure on local carrier lifetime in perovskite solar cells, Science 348 (2015) 683–686, https://doi.org/10.1126/science.aaa5333.
[49] H.-H. Fang, S. Adjokatse, S. Shao, J. Even, M.A. Loi, Long-lived hot-carrier light emission and large blue–shift in formamidinium tin triiodide perovskites, Nat. Commun. 9 (2018) 243, https://doi.org/10.1038/s41467-017-02684-w.
[50] N.K. Noel, S.D. Stranks, A. Abate, C. Wehrenfennig, S. Guarnera, A.-A. Haghighirad, A. Sadhanala, G.E. Eperon, S.K. Pathak, M.B. Johnston, Lead-free organic–inorganic tin halide perovskites for photovoltaic applications, Energy Environ. Sci. 7 (2014) 3061–3068, https://doi.org/10.1039/C4EE01076K.
[51] X. Wu, H. Li, K. Wang, X. Sun, L. Wang, CH 3 NH 3 Pb 1−x Eu x I 3 mixed halide perovskite for hybrid solar cells: the impact of divalent europium doping on efficiency and stability, RSC Adv. 8 (2018) 11095–11101, https://doi.org/10.1039/C7RA12754E.
[52] X. Hu, H. Wang, M. Wang, Z. Zang, Interfacial defects passivation using fullerene-polymer mixing layer for planar-structure perovskite solar cells with negligible hysteresis, Sol. Energy 206 (2020) 816–825, https://doi.org/10.1016/j.solener.2020.06.057.
[53] S. Ippili, V. Jella, J.-H. Eom, J. Kim, S. Hong, J.-S. Choi, V.-D. Tran, N. Van Hieu, Y.-J. Kim, H.-J. Kim, S.-G. Yoon, An eco-friendly flexible piezoelectric energy harvester that delivers high output performance is based on lead-free MASnI 3 films and MASnI3-PVDF composite films, Nano Energy 57 (2019) 911–923, https://doi.org/10.1016/j.nanoen.2019.01.005.
[54] S. Abbasi, X. Wang, P. Tipparak, C. Bhoomanee, P. Ruankham, H. Liu, D. Wongratanaphisan, W. Shen, Proper annealing process for a cost effective and superhydrophobic ambient-atmosphere fabricated perovskite solar cell, Mater. Sci. Semicond. Process. 155 (2023) 107241, https://doi.org/10.1016/j.mssp.2022.107241.
[55] J. Peng, Y. Chen, K. Zheng, T. Pullerits, Z. Liang, Insights into charge carrier dynamics in organo-metal halide perovskites: from neat films to solar cells, Chem. Soc. Rev. 46 (2017) 5714–5729, https://doi.org/10.1039/C6CS00942E.
[56] N.K. Tailor, Yukta, R. Ranjan, S. Ranjan, T. Sharma, A. Singh, A. Garg, K.S. Nalwa, R.K. Gupta, S. Satapathi, The effect of dimensionality on the charge carrier mobility of halide perovskites, J. Mater. Chem. A 9 (2021) 21551–21575, https://doi.org/10.1039/D1TA03749H.